Modeling large nonuniform optical antenna arrays for metasurface application

Tianyu Dong,[1,2,a)] Xikui Ma,[1] and Raj Mittra[2,b)]
[1]*State Key Lab of Electrical Insulation and Power Equipment, School of Electrical Engineering, Xi'an Jiaotong University, Xi'an 710049, China*
[2]*Electromagnetic Communication Laboratory, Department of Electrical Engineering, The Pennsylvania State University, University Park, Pennsylvania 16802, USA*

(Received 8 May 2013; accepted 8 July 2013; published online 23 July 2013)

We analyze large non-uniform optical antenna arrays of nanorods, which form optical vortices, axicons and lenses, by using a numerically efficient technique, called the Characteristics Basis Function Method (CBFM). The efficiency is realized by deriving an accurate, efficient simplified representation of nanorod, and by using the CBFM, which not only reduces the number of unknowns significantly without sacrificing the computational accuracy, but also enables us to handle large, truncated and non-uniform arrays. The method is numerically rigorous and includes all of the mutual coupling effects to obtain accurate results. Furthermore, it is readily parallelizable and can be generalized to handle more complex shapes of nanoantennas, without any difficulty. © *2013 AIP Publishing LLC*. [http://dx.doi.org/10.1063/1.4816351]

I. INTRODUCTION

Metamaterials (MTMs) that are made of subwavelength composites ("meta-atoms") have garnered a lot of attention in recent years, because of their unique electromagnetic properties that are unattainable in nature, with promise of extraordinary functionalities and applications, such as negative refraction[1] and invisibilities.[2,3] Owing to the recent advances in micro- and nano-fabrication techniques, many prototypes of MTM have been demonstrated beyond microwave frequencies, ranging from THz frequencies to infrared and visible wavelengths.[4]

One of the most interesting metastructures is based on the emerging concepts of optical antenna,[5] with applications in solar energy conversion,[6] opto-electronics,[7] biosensing,[8] and imaging,[9] to name a few. For instance, array of optical antennas on a silicon chip can generate accurate pre-defined patterns of light, which could be useful in 3D holography displays and advanced medical imaging.[10]

A special class of MTMs, namely, 2D metamaterials, also called metasurfaces, comprised optical antennas that show promise in controlling electromagnetic waves, e.g., coupling propagating waves to surface waves.[11] More recently, it has been shown that it is possible to direct the light at non-specular angles by controlling the phase dependence of the field scattered at a interface.[12,13] By properly designing and arranging the symmetry-breaking V-shaped optical antennas, it is possible to taper the phase of the scattered field in a desired manner to realize such devices as an optically thin axicon and lens,[14] and a quarter wave plate.[15] Also, observation of giant photonic spin hall effect by virtue of V-shaped antennas has been reported.[16] Additionally, metamorphosing interfacial phase discontinuity ranging from 0 to 2π can also be realized for circularly polarized (CP) waves converted to its opposite helicity.[17,18] Because of their low loss stemming from their ultrathin geometry, metasurfaces can be incorporated into planar photonics; hence, they have the potential to lead to ultrathin devices with a wide variety of functionalities.[19]

Simulation of nano-antennas for metasurfaces, comprising of dispersive metallic nano structures and dielectric environments, plays an important role in the design of metasurface-based devices. A whole host of methods, such as the Finite Element Method (FEM), Finite Difference Time Domain (FDTD) algorithm, Method of Moments (MoM), and the Boundary Element Method (BEM), have been employed for such simulation, after they have been tailored for plasmonic applications.[20–22] Even so, modeling large nano structures still poses great challenges, because unlike uniform phased arrays, or Frequency Selective Surfaces (FSSs), metasurfaces comprise nano-antennas that could in general be different in size, shape, and orientation. Furthermore, the distribution of the elements of the array could either be deterministic, e.g., periodic and aperiodic, or it could be random. As for periodical arrays, such as FSSs, they too could be non-uniform, owing to fabrication tolerances. For such non-periodic geometries, we can no longer solve the problem at hand by considering only a single unit cell—owing to its non-periodic nature—to render the problem manageable. Conventional numerical methods become inefficient when analyzing large arrays and the size they can handle is often limited by the available CPU time and memory. When modeling the behaviors of nano-structures, such as metasurfaces, it is not uncommon to simplify the model by considering a miniaturized structure because of the limitations of the simulation algorithm.[18] Also, mutual coupling effects between the elements in the array are often neglected and other approximations are introduced to render the problem manageable.[14,23]

The objective of the paper is to present a numerically rigorous method to accurately model *finite*, *non-uniform*, and

[a)]Author to whom correspondence should be addressed. Electronic mail: tianyu.dong@gmail.com.
[b)]King Fahd University of Petroleum and Minerals, Dhahran, Saudi Arabia

large plasmonic nanorod arrays, which show promise in designing ultra-thin optical devices.

II. PHASE DISCONTINUITY OF A METASURFACE

We choose plasmonic nanorods for the array elements, with spatially varying angles of orientation, which can generate interfacial phase change for circularly polarized waves,[17] in a manner similar to the symmetry-breaking V-shaped elements,[12,14] which we could also analyze by using the proposed technique. When a circularly polarized wave illuminates a nanorod whose axis has an angle γ with respect to the x axis, the scattered field can be expressed, for small incident and observation angles, as[17]

$$\mathbf{E}^{\text{sca}} \approx E_0(\hat{u}^s + \hat{u}^{-s}e^{\text{i}s2\gamma}), \tag{1}$$

where $s = \pm 1$ denotes the helicity of incident wave ("+", "−" corresponds to right-handed (RCP) and left-handed CPs (LCP), respectively, in accordance with the optical convention); and, $\hat{u}^{\pm s} \approx \hat{x} \pm \text{i}s\hat{y}$ represents the direction of the polarization. It is evident that the opposite polarization has the same amplitude and the interfacial phase discontinuity ϕ can be expressed as

$$\phi = 2\gamma, \tag{2}$$

which only depends on γ, the orientation angle of the nanorod. We can achieve any desired phase distribution by adjusting the orientation of the nanorods, and this property is useful for designing novel reflection- and/or refraction-based optical devices.

III. RESULTS AND DISCUSSIONS

For the first example, we consider an optical vortex formed by plasmonic nanorods. Light can possess orbital angular momentum (OAM), which causes a beam's wavefront to change direction in time. Because of the twisting, the light waves at the axis itself cancel each other out, which focuses the light to donut-shaped contours, rather than at a point, while creating a point of zero intensity at the center. Such properties present novel opportunities for scientific research and technological applications, such as optical tweezing,[24] quantum computing,[25] and cryptography encryption,[26] to name a few.

In order to realize a helical wave front, we introduce an azimuthal phase variation, i.e., $\exp(\text{i}\ell\phi)$, on the metasurface, where ℓ is the topological quantum number (topological charge) and ϕ represents the azimuthal coordinate. Figure 1(a) exhibits the analyzed optical vortex with $\ell = -1$ and Fig. 1(b) shows the corresponding in-plane phase retardation introduced by the metasurface. The array consists of 40×40 nanorods with length of 275 nm and radius of 10 nm that are placed equally spaced across the xoy plane. The separation distance between the centers of the neighboring elements is 500 nm. The orientation angles γ's are determined by using Eq. (2). A RCP Gaussian beam is normally incident from the top, whose waist is located on the metasurface; its radius is 10 nm, and its wavelength is $\lambda = 1.55\,\mu$m.

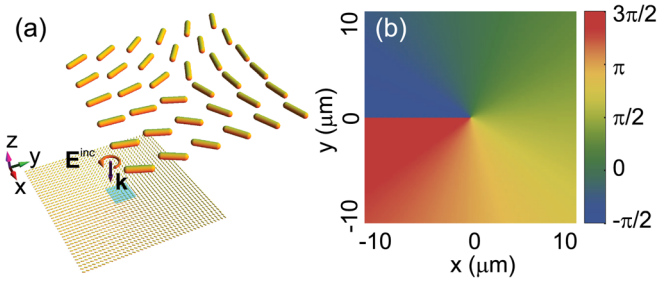

FIG. 1. (a) Schematic of an optical vortex. The nanorods are arranged so as to generate a phase shift that varies from 0 to 2π. (b) Additional interfacial phase dependence introduced by the optical vortex. The topological charge is identified to be $\ell = -1$.

Since such a finite array is obviously non-periodic; hence, it cannot be modeled by using the traditional methods for simulating periodic structures, either by using Floquet theory, which is no longer applicable, or by simply superimposing the contributions of the individual elements since neglecting the mutual coupling effects may introduce unacceptable levels of error. Instead, we use the Characteristic Basis Function Method (CBFM, see details in the Appendix A) by decomposing the domain of the array into N^{BLKs} $(= 40 \times 40 = 1600)$ small blocks, with each block containing only a single nanorod. For each small nanorod, we use a discretization $N_p = 10$, which is quite adequate to represent the nanorod, as demonstrated in Appendix B. We find that the second normalized singular value is 2.3×10^{-3} and the third one drops to 9.0×10^{-5}, inferring that only one primary Characteristic Basis Function (CBF) survives after the singular value decomposition (SVD) procedure if we chose the threshold to be 2.3×10^{-3}. Note that, in this example, since the geometries of each divided elements are uniform except for the orientation, we need only calculate the CBFs for just one block, and use them subsequently for the other blocks without having to recompute them.

We observe the scattered field for the cross-polarized (LCP) components. The observation plane is $120\,\mu\text{m} \times 120\,\mu\text{m}$ large, which is parallel to the metasurface and is located at a distance of $400\,\mu$m below the array. Figure 2(a) displays the intensity pattern calculated by using the CBFM, which is essentially the same as the corresponding result obtained by using the conventional MoM, shown in Fig. 2(c). The relative difference[27] between the two results is found to be is 0.39%. Doughnut-shaped patterns are generated and dark spots are observed at the center which correspond to the phase singularity. The calculated patterns show good agreement with the experimental results reported in Ref. 12. We point out, once again, that the accuracy of the results suffers if we neglect the mutual coupling effects, as is evident from Fig. 2(e). Figures 2(b), 2(d) and 2(f) exhibit the corresponding fringe patterns created by the interference of the vortex beams and co-propagating Gaussian beams, respectively, which identifies the topological charge[28] $\ell = -1$.

For this example, the generation of the CBFs takes a total time 0.62 s, since, as mentioned earlier, we only need to evaluate them for a single block. The time to the reduced impedance matrix takes almost the same time as that needed for the conventional MoM, since only one CBF is retained

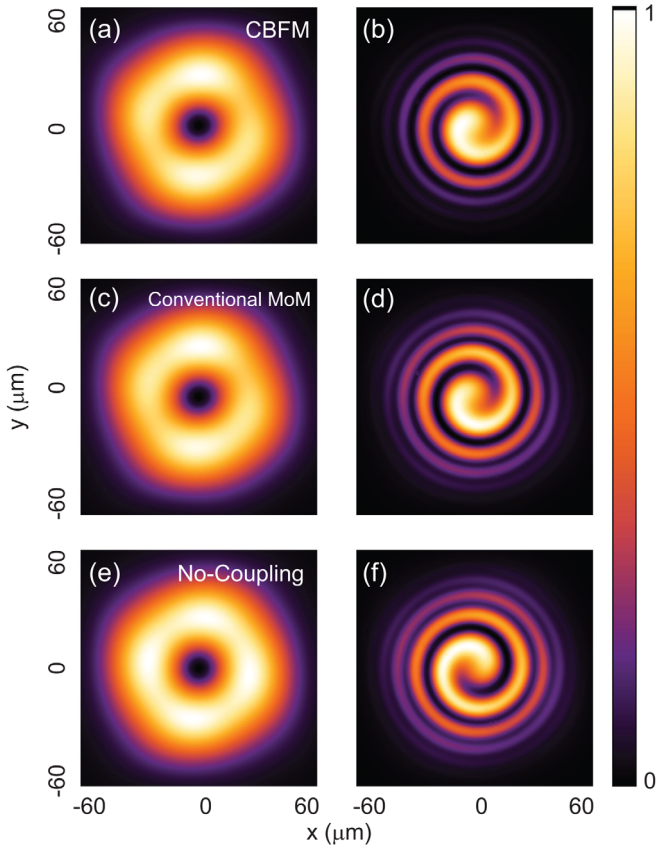

FIG. 2. Far field intensity pattern of an optical vortex carrying topological charge $\ell = -1$, calculated by (a) the CBFM; (c) conventional MoM and (e) neglecting the mutual coupling effects, respectively; (b), (d), and (f), respectively, the calculated interferogram of the vortex beam originated from the corresponding method. The observation plane is located at a distance of 400 μm below the optical vortex array.

after the SVD. Moreover, the CBFM requires 20.48MB ($= 1600 \times 1600 \times 2 \times 4$ bytes, where the factor $\times 2$ arises from the fact that the matrix elements are complex numbers, and the factor $\times 4$ denotes single precision) to store the matrix and 4.5 s to solve the problem. In contrast to this, the conventional MoM consumes 2.048GB of storage and requires 188.6 s of solve-time for the matrix, running on a single processor. We mention that the results in this paper have been generated on the HP ProLiant SL390s G7 Server, which is equipped with 12 Intel X5670 2.93 GHz processors and 48GB of RAM.

In the above configuration, owing to the relative large spacing (500 nm) between the above metasurface transmits through an increased amount of light, and the conversion efficiency is about 1.5% (see Appendix C for details). Since the mutual coupling effects are weak, the results neglecting the mutual coupling effects [see Figs. 2(e) and 2(f)] are not expected noticeably from the results obtained by using the proposed CBFM [see Figs. 2(a) and 2(b)], and those derived by employing the conventional MoM [see Figs. 2(c) and 2(d)]. However, if we decrease the spacing between nanorods from 500 nm to 303 nm, without changing the dimensions of the optical vortex aperture whose size is 20 μm $\times$ 20 μm, the mutual coupling effect would become more significant. We use the same excitation but locate the observation plane at a

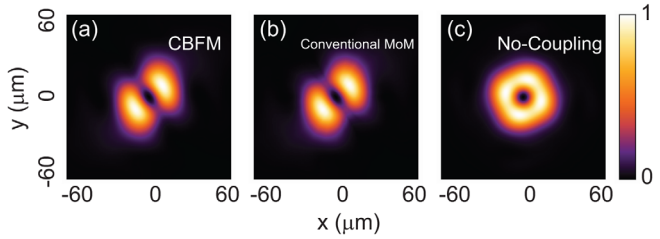

FIG. 3. Far field intensity pattern of an optical vortex carrying topological charge $\ell = -1$, calculated by using (a) the CBFM; (b) conventional MoM and (c) neglecting the mutual coupling effects, respectively. The array has the same size as that analyzed in Fig. 2, while the spacing between nanorods is 303 nm instead of 500 nm. The observation plane is located at a distance of 200 μm below the optical vortex array.

distance of 200 μm below the metasurface, rather than 400 μm as we did previously. As shown in Fig. 3, the field intensity distribution obtained by neglecting the mutual coupling effects [see Fig. 3(c)] is now quite different compared with that obtained from the proposed method [see Fig. 3(a)], which is essentially the same as the result obtained from the conventional MoM [see Fig. 3(b)]. This demonstrates, once again, that neglecting mutual coupling effects may yield inaccurate results and, hence, should be avoided. In addition, it is evident that the dark spot remains at the center as light propagates after impinging on the optical vortices, as shown in Figs. 2 and 3, where the observation planes are located at a distance of 400 μm and 200 μm below the metasurfaces, respectively. Though the aperture size of the optical vortex remains the same, the transmission efficiency of the denser optical vortex array increases to $\sim$3.7% when the spacing is 303 nm.

As illustrated in the Appendix A, dividing the original array into smaller domains can be done in an arbitrary manner; hence, the CBFM can handle perturbations or non-uniform geometries in a natural way, without resorting to approximations. For the next example, we consider an array with a sunflower phyllotaxis pattern, as shown in Fig. 4(a). This metasurface was created by arranging the nanorods such that the n-th nanorod is located at (ρ_n, θ_n), with the coordinates of the location governed by the Fermat's spiral, as follows:

$$\rho_n = L_0\sqrt{n}, \tag{3a}$$

$$\theta_n = ng, \tag{3b}$$

where $g = 2\pi(1 - 1/\varphi)$; φ is the golden ratio; $L_0 = 250$ nm is a scaling constant. There are $N^{\mathrm{BLKs}} = 1600$ nanorods

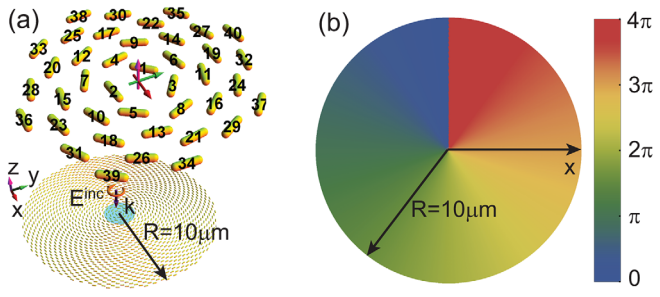

FIG. 4. (a) Schematic of a Fibonacci spiral nanorod array, creating an optical vortex; (b) interfacial phase retardation introduced by the metasurface.

whose orientations are tangential to the spiral. The metasurface also introduces an azimuthal phase gradient, as shown in Fig. 4(b), creating an optical vortex, with $\ell = 2$. Moreover, the radius of the nanorods is 10 nm while their lengths vary *randomly* from 265 nm to 285 nm. The metasurface is illuminated by an LCP Gaussian beam, whose waist radius is $w_0 = 10\mu$m. The wavelength for this simulation is $\lambda = 1.55\mu$m.

In common with the previous example, we first divide the array into $N^{\text{BLKs}} = 1600$ blocks, with each block containing only a single nanorod. Unlike the previous example, we need to generate the CBFs for all blocks because the geometry of each block could be different in general. The generation of CBFs takes 133.4 s for 1600 blocks, when using a server with 12 processors. The far fields of the opposite cross-polarized wave (RCP) are computed over a $200\mu\text{m} \times 200\mu\text{m}$ large plane, at a distance of 400 μm below the metasurface. Figure 5(a) displays the field intensity distribution of the array, derived by using the CBFM, when the lengths of the elements are distributed randomly. The pattern calculated by using the conventional MoM is plotted in Fig. 5(c), derived at a relative high computational cost; yet the difference between the two results is only 0.69%. Figures 5(b) and 5(d) plot the phase distribution of the E_x^{sca} components for the random array, derived by using the CBFM and conventional MoM, respectively. It is evident that the metasurface generates a spiral wavefront, leading to an optical vortex. As a reference, Figs. 5(e) and 5(f) present the intensity pattern and the phase distribution of E_x^{sca}, respectively, for the corresponding metasurface comprising uniform length rods, i.e., $l_0 = 275$ nm. In this example, the calculated conversion efficiency of the array, comprised uniform length nanorods is approximately 3.7%, while it reduces to 2.3% for random length case. This is because some of the nanorod antennas scatter fields at off-resonance frequencies, and this, in turn, reduces the efficiency, as explained in Appendix C.

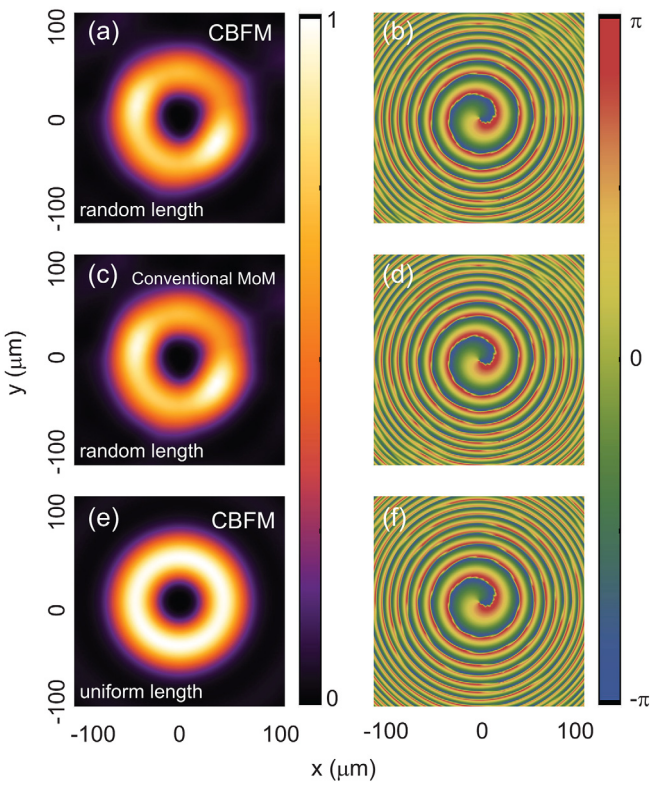

FIG. 5. (a) and (c), respectively, far field intensity distribution of the Fibonacci optical vortex with random length variation of nanorods, calculated by the CBFM and the conventional MoM; (b) and (d) the corresponding phase distribution of E_x^{sca}; (e) and (f) far field intensity pattern and E_x^{sca} phase distribution of the Fibonacci array with an uniform nanorod length ($l_0 = 275$ nm), respectively.

For the third example, we consider an optical axicon,[29] which can create a non-diffractive ring-shaped beam, which retains a constant ring thickness over a radial distance. The axicon can be used to generate an approximation of a Bessel beam with a collimated Gaussian beam input, which is useful for a variety of research and medical application, e.g., corneal surgery,[30] optical coherence tomography,[31] and particle micromanipulation.[32]

Unlike the ultrathin axicon reported in Ref. 14, we use straight nanorods to realize the metasurface, as displayed in Fig. 6. In order to form a conical wavefront of light that travels through the metasurface, the phase delay has to increase linearly with the distance from the center. For a given radius ρ on the metasurface, the phase retardation is to satisfy

$$\phi = \frac{2\pi}{\lambda}\rho \sin\Theta, \tag{4}$$

where $\Theta = \tan^{-1}(R_a/\text{DOF})$, R_a is the radius of the metasurface, and DOF is the depth of focus of the axicon.

We analyze an axicon with a radius of $R_a = 20\mu$m, consisting of N^{BLKs} $(= 5,024)$ nanorods with varying orientations, as determined by using Eqs. (2) and (4). Each nanorod is identical in length, which is 275 nm, and has a radius of 10 nm. The axicon is illuminated by a RCP Gaussian beam, whose waist radius is $w_0 = 40\mu$m; and its wavelength is $\lambda = 1.55\mu$m. Following the approach discussed previously, we simply divide the array into N^{BLKs} smaller problems, each of which consists a single nanorod. As we see from Fig. 7, the reduced impedance matrix is strictly diagonally dominant. Hence, we do not need to perform any permutations while computing an LR factorization. Furthermore, iterative methods, such as the Gauss-Seidel algorithm, are not expected to experience convergence problems, when dealing with such matrices, even if they are large.

Figure 8 plots the computed field intensity of the designed axicon, which is located at $z = 0$. As illustrated in Fig. 8(a) [see the bright bands in the colored figures], light

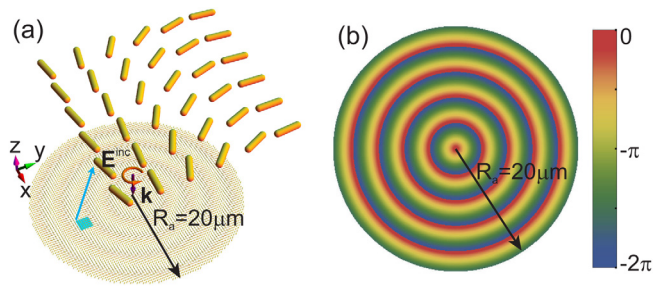

FIG. 6. Schematic showing the design of the axicon. (a) Geometry of the analyzed axicon. (b) The phase profile for the axicon.

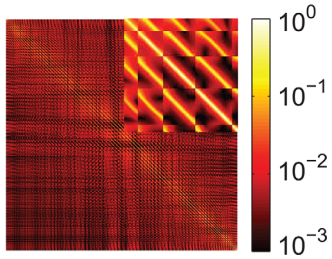

FIG. 7. Modulus of the reduced impedance matrix of dimension $N^{\mathrm{BLKs}} \times N^{\mathrm{BLKs}} = 5024 \times 5024$ for the axicon problem. The inset presents the zoom-in view of the first 100×100 sub matrix. Note that the values of the matrix elements have been normalized to 1.

does not spread out as it propagates within the axicon's depth of focus (DOF = 50 μm), while achieving an approximation of non-diffracting properties. Also, as shown in Fig. 8(b), which displays the intensity distribution at the $z = -33\,\mu$m plane, the beam forms rings of increasing diameters over the radial distance, while preserving their thicknesses, thus closely replicating the properties of a Bessel beam. Figure 8(c) captures the intensity profile along the x-axis of the geometry shown in Fig. 8(b). The calculated conversion efficiency for the simulated axicon is approximately 1.7%.

Finally, to demonstrate the ability of the proposed method to model large plasmonic arrays, we analyze a flat lens comprised $N^{\mathrm{BLKs}} = 31,428$ elements, as depicted in Fig. 9(a). Such an optically thin lens could, in principle, offer the possibility of equipping pint-sized cameras. In order to form a focus at a distance such that all light arrives there in phase, additional phase retardation should be introduced to compensate for the phase lead introduced by the disparity in the physical paths. For a focal length f, the phase dependence ϕ as a function of the radius of ρ can be expressed as

$$\phi = \frac{2\pi}{\lambda}\left(\sqrt{\rho^2 + f^2} - f\right), \tag{5}$$

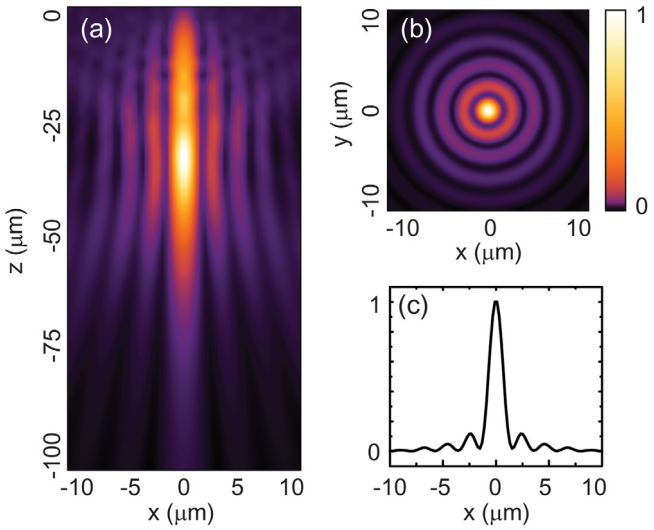

FIG. 8. Calculations results by using the CBFM. The results showing the (a) xz (longitudinal) and (b) xy (lateral) cross sections of the far-field intensity distributions. (c) Plots of the intensity along the x axis on $y = 0$, $z = -33\,\mu$m plane. Note that a square-root color scale is used for the far-field intensity distributions in (a) and (b).

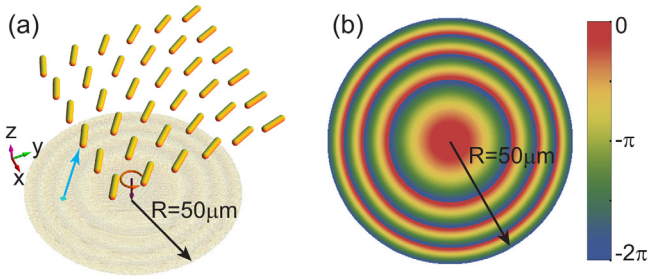

FIG. 9. (a) Schematic of the design of the lens with a focus of 200 μm. (b) Hyperboloidal radial phase distribution introduced by the metasurface.

which correspond to hyperboloidal type of radial phase distribution, as shown in Fig. 9(b). Once the phase profile has been determined, the orientation angles can be obtained from Eq. (2).

The lens, whose diameter is 100 μm, is located at the $z = 0$ plane, and its designed focal length is $f = 200\,\mu$m. It is illuminated by an RCP plane wave whose wavelength is $\lambda = 1.55\mu$m. Figure 10 shows the results calculated by using the CBFM. As we see from Fig. 10(a), light is confined to the focal region for the normal incidence case, as desired. Because the array is finite, the maximum of the spot is located at $z = -196.1\,\mu$m, rather than the designed value $z = -200\,\mu$m. Once the reduced impedance has been filled, we can solve for multiple excitations by using the same matrix, without generating a new one for each incident angle, which, in turn, results in significant time saving. Figure 10(b) plots the field intensity of the xz cut-plane of the meta-lens at

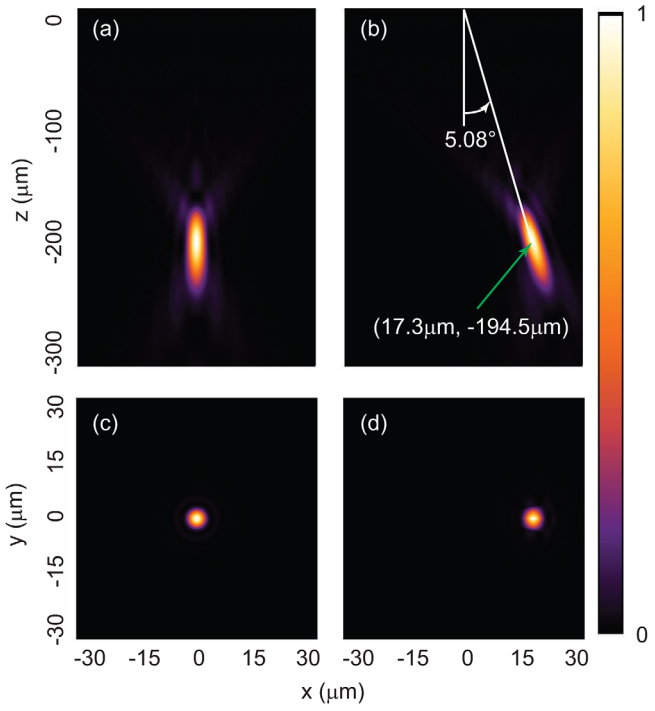

FIG. 10. Calculations results for the lens by using the CBFM. Longitudinal cross section of the field distribution for the (a) normal incidence and (b) oblique incidence, respectively. The same reduced impedance matrix is used for multiple excitations, lending to considerable time-saving. (c) and (d) Transverse cross sections of the field distribution at the spots corresponding to (a) and (b), respectively.

$y = 0$, for the oblique incident angle $\theta^{\text{inc}} = 5°$. We observe that the focal beam tilts as desired. Figures 10(c) and 10(d) show the corresponding xy cross-section of the field distribution at the spots. The calculated conversion efficiency for the simulated lens is about 1.9%.

If we were to use the conventional method and $N_p = 10$ unknowns for each element, it would require $[31,428 \times 10 \times (31,428 \times 10 + 1)/2] \times 2 \times 4$ bytes $\approx$ 395GB of memory to store the impedance matrix, even when we use only single precision, and only store the upper triangular part of the impedance matrix by taking advantage of the symmetry property of the matrix. Furthermore, the solve-time of the matrix would increase dramatically, since it behaves as $\mathcal{O}[(N^{\text{BLKs}} \cdot N_p)^3]$. In contrast to this, only $[31,428 \times 1 \times (31,428 \times 1 + 1)/2] \times 2 \times 4$ bytes $\approx$ 3.95GB of memory is needed to store the reduced impedance matrix, since only a single post-SVD CBF survives and N_p^{CBFs} is only 1. Solving the reduced matrix takes only about 6 min on a single processor. Presently, without any optimization, filling the reduced impedance matrix is the most time-consuming part in our simulation. However, it is worthwhile to point out that it is possible to accelerate this step significantly, e.g., by using fast matrix generation techniques.[33,34] In addition, both the complexity as well as the CPU time could be further reduced by sub-dividing the array into a smaller number of blocks and employing the sparse matrix algorithm.[35] We plan to explore these avenues in the future.

IV. CONCLUSIONS

In this paper, we have introduced a computationally efficient algorithm, called the CBFM, which reduces both the CPU time and the memory to render large problems manageable. We have used this algorithm to analyze *large non-uniform* plasmonic antenna arrays for metasurface applications, including optical vortices, axicons and lenses. We have demonstrated that the use of thin-wire type of approximation for the nanorod, for the case when the aspect ratio of the length of the nanorod and its diameter is large, increases the computational efficiency significantly without sacrificing the accuracy, as we have shown by comparing the present results with those derived by using commercial FEM simulations. We have also demonstrated that the proposed method is accurate as well as efficient for modeling nonuniform arrays, and has the capability of handling very large arrays in a numerically efficient manner. The proposed method lends itself to convenient parallelization, which enables one to reduce the CPU run-time even further by utilizing multiple processors. The method presented herein can be readily generalized to handle arrays comprised nanoantennas with complex shapes, and is suitable for rapid designing of metasurfaces for a variety of applications.

ACKNOWLEDGMENTS

Tianyu Dong would like to thank Dr. Giacomo Bianconi and Dr. Chiara Pelletti for fruitful discussions on CBFM and its parallelization. He also acknowledges the Chinese Scholarship Council (CSC) and the Graduate School of Xi'an Jiaotong University, which sponsored him to carry out this research at the EMC Lab of Penn State.

APPENDIX A: CBFM

The conventional MoM needs to solve a dense, complex linear system of equations, and the associated impedance matrix Z has the dimensions of $N \times N$, where N is the number of unknowns. The burdens of storage and CPU time increase as $\mathcal{O}(N^2)$ and $\mathcal{O}(N^3)$, respectively, with the number of degrees of freedom (DoFs) N. As the dimension of the array increases, the conventional MoM faces a considerable burden when handling large matrices and attempts to reduce this burden by neglecting the mutual coupling effects leads to inaccurate results, as we have pointed out before in Sec. III. Moreover, the large size matrices are not tractable by direct solvers, while using iterative methods often leads to convergence problems because the matrix is ill-conditioned.

In contrast to the conventional approach to dealing with large problems directly solving the entire array, as shown in Fig. 11(a), which leads to a large number of unknowns, the CBFM[35,36] begins by dividing the original large array into several blocks, say N^{BLKs}, where the unknown current distribution in each block is represented in terms of macro-basis functions, called the CBFs, and this enables us to use the direct solvers once again, even for very large problems. To generate the CBFs, each block is illuminated by a set of plane waves, with both the TE and TM polorizations that impinge on the block at different incident angles covering the entire 360°, as shown in Fig. 11(b). The number of incident angles (N_p^{inc}) is deliberately chosen to be greater than the number of unknowns (N_p) for each block ($N_p^{\text{inc}} > N_p$), so that the CBFs, so constructed, could be used later for waves incident at an arbitrary angle, without having to regenerate them. Next, the set of current distribution is obtained for different angles for each small problem by solving the matrix equations

$$\mathbf{Z}_p \mathbf{I}_{p,q} = \mathbf{V}_{p,q}, \quad p = 1 \ldots N^{\text{BLKs}}, \quad q = 1 \ldots N_p^{\text{inc}}, \qquad \text{(A1)}$$

where $\mathbf{Z}_p$ is an $N_p \times N_p$ matrix.

Next, in order to derive the primary CBFs, an SVD algorithm is employed to eliminate the redundant solutions, and to retain only a few linearly independent CBFs that survive, say

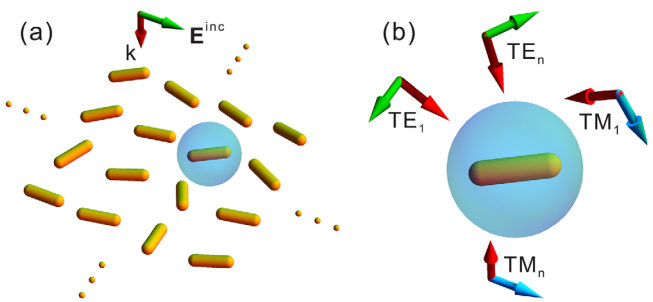

FIG. 11. Demonstration of the characteristic basis function method. (a) A finite non-uniform array is illuminated by an arbitrary polarized wave; (b) each element is isolated and illuminated by a bunch of plane waves with different angles for both polarizations. The number of incident waves should be overestimated to get the primary CBFs.

$\mathbf{I}_{p,q}^{\mathrm{CBF}}$, which represents the q-th CBF for the p-th block. It is worthwhile to mention that, in general, the normalized singular values decrease rapidly, with a sharp cutoff, once they go down below a certain threshold.[35] As a result, the number of post-SVD CBFs, N_p^{CBFs}, is relatively small, typically much smaller than the number of unknowns N_p, i.e., $N_p^{\mathrm{CBFs}} \ll N_p$.

In common with the conventional MoM, the current distribution on the rods can be expanded as a linear combination of these CBFs, as follows:

$$\mathbf{I}(u) = \sum_{p=1}^{N^{\mathrm{BLKs}}} \sum_{q=1}^{N_p^{\mathrm{CBFs}}} \alpha_{pq} \mathbf{I}_{p,q}^{\mathrm{CBF}}(u), \tag{A2}$$

where α_{pq} represents the unknown weight of the q-th CBF for the p-th element. Next, to obtain these weights, we construct a reduced impedance matrix, by following the usual recipe for the conventional MoM, except that we use the generated CBFs $\mathbf{I}_{p,q}^{\mathrm{CBF}}(u)$ for the basis and testing functions, rather than the low-level basis functions. This leads us to the equation for the reduced matrix

$$[Z_{p'q',pq}^{\mathrm{reduced}}][\alpha_{pq}] = [V_{p'q'}^{\mathrm{reduced}}], \tag{A3}$$

where

$$Z_{p'q',pq}^{\mathrm{reduced}} = \langle \mathbf{I}_{p',q'}^{\mathrm{CBF}}, \mathbf{Z}_{q'q} \cdot \mathbf{I}_{p,q}^{\mathrm{CBF}} \rangle, \tag{A4}$$

and

$$V_{p'q'}^{\mathrm{reduced}} = -\langle \mathbf{I}_{p',q'}^{\mathrm{CBF}}, \mathbf{E}_{q'}^{\mathrm{inc}} \rangle. \tag{A5}$$

In Eq. (A4), $\mathbf{Z}_{q'q}$ is the sub-coupling matrix of the original conventional MoM, which links the blocks q' and q; and $\langle \cdot, \cdot \rangle$ represents the inner product defined on the corresponding blocks. Finally, the solution of the reduced matrix $\mathbf{Z}_{p'q',pq}^{\mathrm{reduced}}$ yields the desired weights α_{pq} that we are seeking.

The use of the CBFM reduces the computational burden of the original problem when we follow the above procedure, which involves (i) solving N^{BLKs} small problems with $N^{\mathrm{BLKs}}\mathcal{O}(N_p^3)$ operation complexity and generating the corresponding primary CBFs, which is highly parallelizable because each block can be analyzed separately; (ii) filling the reduced impedance matrix according to Eq. (A4); and (iii) solving the reduced matrix Eq. (A3) for particular excitations given by Eq. (A5) to obtain the current distribution on the nanorods of the array. We reiterate the fact that filling the reduced matrix can be accelerated, by using techniques, such as sparse matrix approach,[35] where only the "near-field" interactions are included. The complexity of solving the entire problem in memory and CPU time reduces from $\mathcal{O}[(N^{\mathrm{BLKs}} \cdot N_p)^2]$ and $\mathcal{O}[(P \cdot N_p)^3]$ to $\mathcal{O}[(N^{\mathrm{BLKs}} \cdot N_p^{\mathrm{CBFs}})^2]$ and $\mathcal{O}[(N^{\mathrm{BLKs}} \cdot N_p^{\mathrm{CBFs}})^3]$, respectively, because $N_p^{\mathrm{CBFs}} \ll N_p$, typically by orders of magnitude. Furthermore, techniques, such as the Adaptive Cross Approximation (ACA), can also be incorporated to further reduce the memory requirements and CPU time needed to solve the reduced matrix problem.[37]

In summary, compared with the well-established conventional MoM based Characteristic Basis Function Method proposed herein has several advantages: (i) it splits the original problem into smaller sub problems and forms much smaller "impedance matrix", resulting in a less memory requirement for storage and a reduction in CPU time for solving linear equations; (ii) the splitting processing is arbitrary, which implies the proposed method is highly parallelizable, hence it can be accelerated by utilizing multiple processors; (iii) the mutual coupling effects between antennas are rigorously included regardless of the decomposition of the geometry, improving the accuracy of the results; (iv) the proposed technique handles non-periodic plasmonic configurations in a natural way without an increase in the complexity; (v) when the antennas have a simple geometry, such as nanorods, the number of characteristic bases are relatively small, which further reduces the complexity of the original problem. An efficient and accentuate representation for nanorods is introduced in the Appendix B below.

APPENDIX B: ONE-DIMENSIONAL REPRESENTATION OF THE INDUCED CURRENT ON A NANOROD

The geometry considered in this paper is that of nanorod, as displayed in Fig. 12(a), whose length and radius are l_0 and r_0, respectively. If the aspect ratio $2r_0/l_0$ is sufficiently small ($r_0 \ll l_0$), the axial current flow is the dominant component and the current flow in the lateral direction, as well as the transverse components of the current density, can be neglected. Furthermore, it can be assumed that the current density distribution is uniform across the cross section of the nanorod. Under these approximations, we can use the thin wire model for the nanorod,[38,39] and the boundary condition, $\mathbf{J}(\mathbf{r}) = \sigma \mathbf{E}^{\mathrm{tot}}(\mathbf{r})$, can be rewritten as

$$-\mathrm{i}\omega\epsilon_0(\epsilon_r - 1)[\mathbf{E}^{\mathrm{inc}} + \mathbf{E}^{\mathrm{sca}}] = \mathbf{I}(u)/(\pi r_0^2), \tag{B1}$$

where the volume current density $\mathbf{J}(\mathbf{r})$ reduces to a line current $\mathbf{I}(u)$ flowing along the axis of the nanorod [see the black (solid) line in Fig. 12(b)].

In order to numerically solve Eq. (B1), the nanorod is discretized into N segments, as shown in Fig. 13(a). Next, the axial current $\mathbf{I}(u)$ is expanded as a summation of the basis functions $b_n(u)$, as follows:

$$\mathbf{I}(u) = \sum_{n=0}^{N} \hat{u}_n I_n b_n(u), \tag{B2}$$

where I_n is the n-th unknown coefficient, and $\hat{u}_n$ represents the current direction at the n-th segment. It is well known that the metals are no longer perfect electric conductors

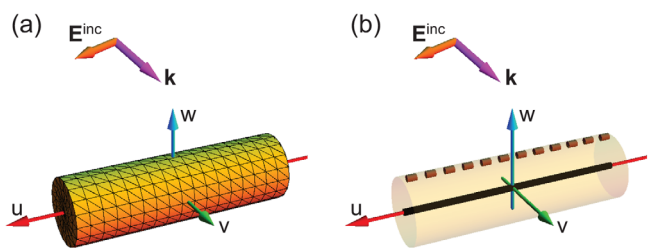

FIG. 12. (a) MoM or BEM representation of a single nanorod; (b) one dimensional (thin-wire) approximation of a nanorod.

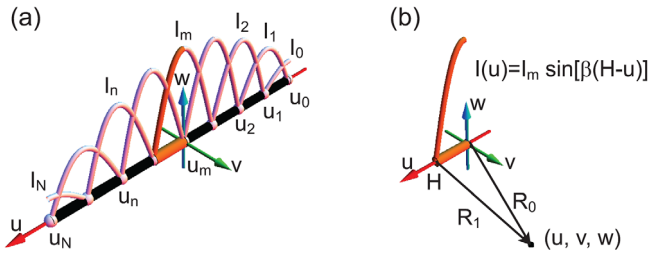

FIG. 13. (a) Mesh and basis functions for MoM; (b) half-sinusoidal short dipole current radiation.

(PECs), but are plasmonic in nature at infrared and optical frequencies. Hence, the case of PEC rods for which current vanishes at the end of the rods, the current distribution on a nanorod does not go to zero at the end, but it supports additional charges instead. Although the choice of basis functions is somewhat arbitrary, certain choices for these functions enhance the numerical efficiency of the method. For this reason, instead of choosing delta functions for bases as was done in Ref. 38, our choice for the basis b_n is the sinusoidal function, as defined below:

$$b_n(u) = \sin[\beta(H - |u - u_n|)], \quad u_{n-1} \le u \le u_{n+1}, \tag{B3}$$

where β is the propagation constant of the surface charge wave.[40] The reason for making this choice is that it leads to an analytical expression for the radiated field, in a convenient manner, bypassing the need to evaluate it by performing a convolution with the dyadic Green's function. Note that Eq. (B3) is still valid for the first and last segment, if we define $u_{-1} = u_0$ and $u_{N+1} = u_N$, respectively.

As shown in Fig. 13(b), a u-directed short current filament of length H is located at the origin of a cartesian $\{u, v, w\}$-coordinates, which carries a half-sinusoidal current distribution

$$\mathbf{I}(u) = \hat{u} I_m \sin[\beta(H - u)], \quad 0 \le u \le H, \tag{B4}$$

and its radiated fields at a point (u, v, w) are given by

$$E_u = \frac{\mathrm{i} I_m \eta}{4\pi}\left[\frac{e^{\mathrm{i}\beta R_1}}{R_1} - \cos(\beta H)\frac{e^{\mathrm{i}\beta R_0}}{R_0} - u\sin(\beta H)(1 - \mathrm{i}\beta R_0)\frac{e^{\mathrm{i}\beta R_0}}{\beta R_0^3}\right], \tag{B5a}$$

and

$$E_{v|w} = \frac{-\mathrm{i} I_m \eta v|w}{4\pi(v^2 + w^2)} \cdot \left\{(u - H)\frac{e^{\mathrm{i}\beta R_1}}{R_1} - u\cos(\beta H)\frac{e^{\mathrm{i}\beta R_0}}{R_0} + \sin(\beta H)[\mathrm{i}\beta R_0 u^2 + (v^2 + w^2)]\frac{e^{\mathrm{i}\beta R_0}}{\beta R_0^3}\right\}, \tag{B5b}$$

where η denotes the wave impedance; $R_0 = \sqrt{u^2 + w^2 + w^2}$ and $R_1 = \sqrt{(u - H)^2 + v^2 + w^2}$.

Next, we apply the Galerkin method to the Eq. (B1). By evaluating the inner product of the basis functions $\hat{u}_m b_m(u)$ and both sides of Eq. (B1), on the interval $[u_{m-1}, u_{m+1}]$, we can obtain $N + 1$ linear equations with $N + 1$ unknowns I_n, which read

$$[Z_{mn}][I_n] = [V_m], \tag{B6}$$

where the elements Z_{mn} of matrix are given by

$$Z_{mn} = \begin{cases} \int_{u_{m-1}}^{u_{m+1}} \hat{u}_m b_m(u) \cdot \mathbf{E}^{\mathrm{sca}}_{mm}(u)\mathrm{d}u \\ \quad + \dfrac{\int_{u_{m-1}}^{u_{m+1}} [b_m(u)]^2 \mathrm{d}u}{\mathrm{i}\omega\epsilon_0(\epsilon_r - 1)\pi r_0^2}, & m = n \\ \int_{u_{m-1}}^{u_{m+1}} \hat{u}_m b_m(u) \cdot \mathbf{E}^{\mathrm{sca}}_{mn}(u)\mathrm{d}u \\ \quad + \dfrac{\int_{u_m}^{u_n} \hat{u}_m b_m(u) \cdot \hat{u}_n b_n(u)\mathrm{d}u}{\mathrm{i}\omega\epsilon_0(\epsilon_r - 1)\pi r_0^2}, & |m - n| = 1 \\ \int_{u_{m-1}}^{u_{m+1}} \hat{u}_m b_m(u) \cdot \mathbf{E}^{\mathrm{sca}}_{mn}(u)\mathrm{d}u, & \text{others}, \end{cases} \tag{B7}$$

and

$$V_m = -\int_{u_{m-1}}^{u_{m+1}} \hat{u}_m b_m(u) \cdot \mathbf{E}^{\mathrm{inc}}_m(u)\mathrm{d}u. \tag{B8}$$

In Eq. (B7), $\mathbf{E}^{\mathrm{sca}}_{mn}(u)$ is the scattered field at the m-th segment which is radiated by the n-th piecewise sinusoidal current segment $\hat{u}_n b_n(u)$ (basis function), and which can be evaluated analytically by using Eq. (B5). It should be mentioned that, in order to avoid the singularities when evaluating the fields which radiated by itself in Eq. (B5), the boundary conditions are applied on the surface of the nanorod, as depicted by the brown (dashed) line in Fig. 12(b), while the current is assumed to be located at the center of the rod.

To verify our approximation, we analyze a gold nanorod with a length of $l_0 = 275$nm and a radius of $r_0 = 10$nm. The nanorod is located at the origin and is aligned in x-direction. An x-polarized plane wave is assumed to be incident from the z-direction. The scattered electric field is observed at the point (0, 0, 1 μm). Figure 14 plots the frequency responses, computed by the proposed method, and by the commercial

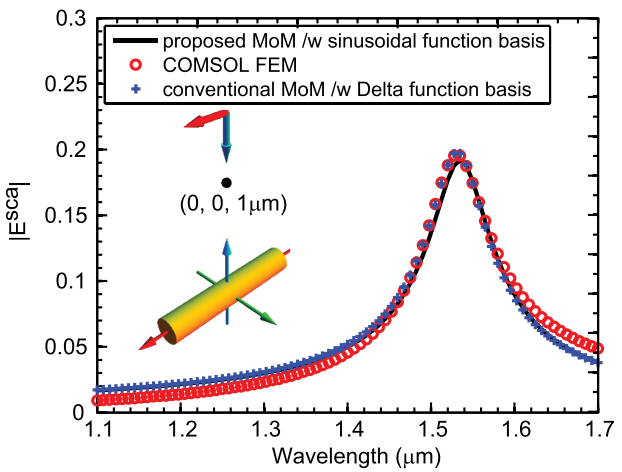

FIG. 14. Comparison among the results obtained by using the simplified method of moments with the utilization of sinusoidal base functions, the commercial finite element method (COMSOL MULTIPHYSICS), and the conventional method of moments with the employment of Delta basis functions.

finite element method solver, COMSOL MULTIPHYSICS, as well as by the conventional MoM with Delta base function,[38] respectively. It is evident that the three responses agree very well with each other. However, in contrast to the number of DoFs which is 5.5×10^5, in COMSOL, our MoM based method proposed herein only needs 10 unknowns, while the conventional MoM needs more than 50 unknowns. One consequence of this is that the simulation using the approximation takes about 3 s for 41 frequency samples, as compared with ~8 h required by COMSOL and ~8 s required by the conventional MoM with Delta base function.

Figure 15 further compares the thin-wire representation, employing the sinusoidal base functions proposed herein, and the Delta base function, that were used in Ref. 38. Figure 15(a) shows that, when the number of DOFs is greater than 3, the use of sinusoidal basis functions used herein achieves consistent results as the number of DOFs is increased, and the results consistent with those obtained from the commercial FEM code, as shown in Fig. 14, because the sinusoidal basis functions are able to accurately represent the current distribution.[41] However, when the Delta base function is used, the calculated frequency response of the scattered field exhibits a red-shift as we increase the mesh density, as is evident from Fig. 15(b). This is because that smaller the mesh size, the fatter are the line segments used to represent the nanorod, and the nanorod appears to be longer than its physical length if the same radius is used. Hence, the resonance red-shift occurs when the number of DOFs is increased, since the simulated nanorod becomes longer. Furthermore, in order to get the same results, the proposed approach presented herein, requires much fewer DOFs to represent the nanorod, usually by orders of magnitude, and it requires much less memory than that needed when we employ Delta function type of basis.

Note that, we use the Drude model for gold, given by

$$\epsilon_r(\omega) = \epsilon_\infty - \frac{\omega_p^2}{\omega^2 + \mathrm{i}\omega\gamma_p}, \tag{B9}$$

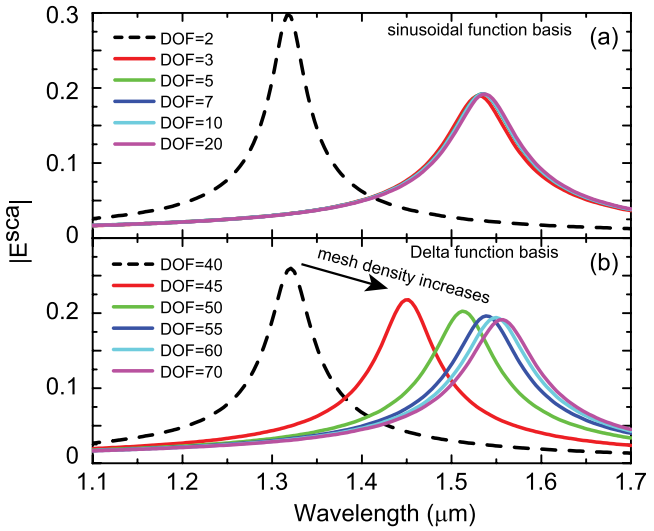

FIG. 15. Comparison between the results obtained by using the method of moments with employment of (a) the sinusoidal basis functions and (b) the Delta basis functions, respectively, where different number of degrees of freedoms are used.

where $\epsilon_\infty = 9.5$, $\hbar\omega_p = 8.95\,\mathrm{eV}$, and $\hbar\gamma_p = 0.069\,\mathrm{eV}$ ($\hbar$ is the reduced Planck's constant). We mention here that these parameters have been retrieved from Ref. 42.

APPENDIX C: CONVERSION EFFICIENCY OF METASURFACES

Figure 16 shows the energy flow when a metasurface is illuminated by circularly polarized waves. As pointed out in Sec. II, the scattered field of a nanorod, illuminated by a circularly polarized field, comprised two main parts. The first one of these with the opposite helicity provides the phase discontinuity which only depends on the rotation angle. The second, with the same helicity, does not contribute to the artificial phase variation, and is filtered out. Consequently, the conversion efficiency of such metasurfaces is limited. In our simulation, numerical polarization filters are used after lights go through the metasurfaces. Besides the reflected and transmitted waves, antennas themselves absorb energy. The conversion efficiency further reduces because the metallic antennas are lossy at the infrared frequencies, as implied by the Drude model [see Eq. (B9) in the Appendix B].

In order to calculate the conversion efficiency, or the transmission efficiency, we can simply calculate the incident power flow across the metasurface area, and we integrate the Poynting vector of the cross polarized components over a cross section parallel to the metasurface (probe surface) after lights go through it. That is,

$$\eta_{\text{efficiency}} = \frac{P|_{\text{probe surface}}}{P|_{\text{metasurface area}}}, \tag{C1}$$

where $P = \int_A \hat{n} \cdot \mathbf{S}\mathrm{d}A$ represents the power through the surface A; $\hat{n}$ is the norm vector of A; $\mathbf{S} = 0.5 \times \mathrm{Re}[\mathbf{E} \times \mathbf{H}^*]$ represents the Poynting vector; and the superscript $(\cdot)^*$ denotes a conjugation. Once the current distribution of the metasurface is determined, the scattered electric field at any location, whether it is located near or far from the array, can be obtained by using Eq. (B5). Similarly, the magnetic fields radiated by the same current filament [see Appendix B], as shown in Fig. 13(b), are given by

$$H_u = 0, \tag{C2a}$$

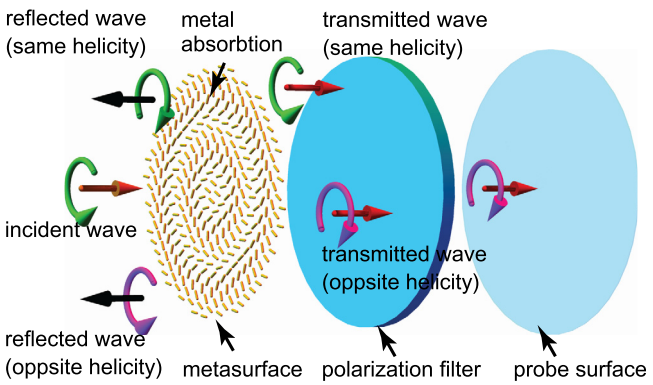

FIG. 16. Power flow of lights after impinging on a metasurface comprised nanorods with different orientation angles.

$$H_v = \frac{wI_m}{4\pi\beta(v^2+w^2)}\left[\frac{e^{i\beta R_1}}{R_1} - \cos(\beta H)\frac{e^{i\beta R_0}}{R_0} + i\cdot 2u\sin(\beta H)\frac{e^{i\beta R_0}}{R_0^2}\right], \quad \text{(C2b)}$$

and

$$H_w = -\frac{vI_m}{4\pi\beta(v^2+w^2)}\left[\frac{e^{i\beta R_1}}{R_1} - \cos(\beta H)\frac{e^{i\beta R_0}}{R_0} + i\cdot 2u\sin(\beta H)\frac{e^{i\beta R_0}}{R_0^2}\right]. \quad \text{(C2c)}$$

In our simulations, we have Gaussian beam illumination, and, hence, the input energy is confined within a certain region instead of spreading over the entire space. After light goes through the arrays and the polarization filters, it is confined within a bounded region, for all the simulated metasurfaces of interest here, viz., optical vortices, axicons and lenses. Hence, the probe surface does not need to be too large to capture the power converted by the metasurfaces.

Since the scattering amplitudes of light of the opposite helicity are identical [see Eq. (1)], the conversion efficiency of the opposite polarization is independent to the orientation of the nanorods, but is determined by the geometry, and the efficiency is the highest at the resonance point of the nanorods. One may increase the transmission efficiency by using low loss metals or by decreasing the spacing between the antennas. In the latter case, the mutual coupling effects become significant, and our proposed method herein provides a rigorous and efficiency way to render such problems manageable and also reduces the computational burden significantly.

[1]J. B. Pendry, Phys. Rev. Lett. **85**, 3966 (2000).
[2]J. B. Pendry, D. Schurig, and D. R. Smith, Science **312**, 1780 (2006).
[3]U. Leonhardt, Science **312**, 1777 (2006).
[4]N. I. Zheludev and Y. S. Kivshar, Nature Mater. **11**, 917 (2012).
[5]P. Bharadwaj, B. Deutsch, and L. Novotny, Adv. Opt. Photon. **1**, 438 (2009).
[6]S. Linic, P. Christopher, and D. B. Ingram, Nature Mater. **10**, 911 (2011).
[7]S. Armstrong, Nat. Photonics **6**, 716 (2012).
[8]M. Käll, Nat. Nanotechnol. **7**, 347 (2012).
[9]J. Chen, M. Badioli, P. Alonso-González, S. Thongrattanasiri, F. Huth, J. Osmond, M. Spasenović, A. Centeno, A. Pesquera, P. Godignon, A. Z. Elorza, N. Camara, F. Javier García de Abajo, R. Hillenbrand, and F. H. L. Koppens, Nature **487**, 77 (2012).
[10]J. Sun, E. Timurdogan, A. Yaacobi, E. S. Hosseini, and M. R. Watts, Nature **493**, 195 (2013).
[11]S. Sun, Q. He, S. Xiao, Q. Xu, X. Li, and L. Zhou, Nature Mater. **11**, 426 (2012).
[12]N. Yu, P. Genevet, M. A. Kats, F. Aieta, J. P. Tetienne, F. Capasso, and Z. Gaburro, Science **334**, 333 (2011).
[13]X. Ni, N. K. Emani, A. V. Kildishev, A. Boltasseva, and V. M. Shalaev, Science **335**, 427 (2012).
[14]F. Aieta, P. Genevet, M. A. Kats, N. Yu, R. Blanchard, Z. Gaburro, and F. Capasso, Nano Lett. **12**, 4932 (2012).
[15]N. Yu, F. Aieta, P. Genevet, M. A. Kats, Z. Gaburro, and F. Capasso, Nano Lett. **12**, 6328 (2012).
[16]X. Yin, Z. Ye, J. Rho, Y. Wang, and X. Zhang, Science **339**, 1405 (2013).
[17]L. Huang, X. Chen, H. Mühlenbernd, G. Li, B. Bai, Q. Tan, G. Jin, T. Zentgraf, and S. Zhang, Nano Lett. **12**, 5750 (2012).
[18]X. Chen, L. Huang, H. Mühlenbernd, G. Li, B. Bai, Q. Tan, G. Jin, C. Qiu, S. Zhang, and T. Zentgraf, Nat. Commun. **3**, 1198 (2012).
[19]A. V. Kildishev, A. Boltasseva, and V. M. Shalaev, Science **339**, 1232009 (2013).
[20]J. Smajic, C. Hafner, L. Raguin, K. Tavzarashvili, and M. Mishrikey, J. Comput. Theor. Nanosci. **6**, 763 (2009).
[21]A. Rashidi and H. Mosallaei, Appl. Phys. Lett. **101**, 061105 (2012).
[22]F. J. García de Abajo and A. Howie, Phys. Rev. B **65**, 115418 (2002).
[23]J. P. Tetienne, R. Blanchard, N. Yu, P. Genevet, M. A. Kats, J. A. Fan, T. Edamura, S. Furuta, M. Yamanishi, and F. Capasso, New J. Phys. **13**, 053057 (2011).
[24]G. Molina-Terriza, J. P. Torres, and L. Torner, Nat. Phys. **3**, 305 (2007).
[25]X. Cai, J. Wang, M. J. Strain, B. Johnson-Morris, J. Zhu, M. Sorel, J. L. O'Brien, M. G. Thompson, and S. Yu, Science **338**, 363 (2012).
[26]G. Gibson, J. Courtial, M. J. Padgett, M. Vasnetsov, V. Pas'ko, S. M. Barnett, and S. Franke-Arnold, Opt. Express **12**, 5448 (2004).
[27]The relative difference is defined as $\delta_{\text{difference}} = ||\mathbf{E}^2_{\text{CBFM}} - \mathbf{E}^2_{\text{Conv.MoM}}||_2 / ||\mathbf{E}^2_{\text{Conv.MoM}}||_2$, where $\mathbf{E}^2$ represents the electric field intensity and $||\cdot||_2$ denotes the 2-norm of the matrix of the intensity distribution.
[28]N. R. Heckenberg, R. McDuff, C. P. Smith, and A. G. White, Opt. Lett. **17**, 221 (1992).
[29]J. H. McLeod, J. Opt. Soc. Am. **44**, 592 (1954).
[30]W. W. Haw and E. E. Manche, J. Refractive Surg. **16**, 724 (2000); available at http://citeseerx.ist.psu.edu/viewdoc/download?doi=10.1.1.33.5623&rep=rep1&type=pdf.
[31]Z. Ding, H. Ren, Y. Zhao, J. S. Nelson, and Z. Chen, Opt. Lett. **27**, 243 (2002).
[32]V. Garcés-Chávez, D. McGloin, H. Melville, W. Sibbett, and K. Dholakia, Nature **419**, 145 (2002).
[33]C. Pelletti, G. Bianconi, R. Mittra, A. Monorchio, and K. Panayappan, IET Proc. Microwaves, Antennas Propag. **6**, 46 (2012).
[34]S. J. Kwon and R. Mittra, Microwave Opt. Technol. Lett. **51**, 204 (2009).
[35]E. Lucente, A. Monorchio, and R. Mittra, IEEE Trans. Antennas Propag. **56**, 999 (2008).
[36]V. V. S. Prakash and R. Mittra, Microwave Opt. Technol. Lett. **36**, 95 (2003).
[37]R. Maaskant, R. Mittra, and A. Tijhuis, IEEE Trans. Antennas Propag. **56**, 3440 (2008).
[38]R. Blanchard, G. Aoust, P. Genevet, N. Yu, M. A. Kats, Z. Gaburro, and F. Capasso, Phys. Rev. B **85**, 155457 (2012).
[39]A. Rashidi, H. Mosallaei, and R. Mittra, J. Appl. Phys. **109**, 123109 (2011).
[40]L. Novotny, Phys. Rev. Lett. **98**, 266802 (2007).
[41]E. K. Miller and F. J. Deadrick, "Topics in applied physics," in *Numerical and Asymptotic Techniques in Electromagnetics*, edited by R. Mittra (Springer, Berlin, Heidelberg, 1975), Vol. 3, pp. 89–127.
[42]P. B. Johnson and R. W. Christy, Phys. Rev. B **6**, 4370 (1972).